Positive cooperativity between RAS-binding and cysteine-rich domains regulates RAF membrane binding kinetics via lateral rebinding

Andres Jimenez Salinas,[1,‡] Kesaria Tevdorashvili,[1,‡] Julian Grim,[1] Alexia Morales,[1] Ani Chakhrakia,[1] & Young Kwang Lee[1,2*]

[1]Department of Chemistry and Biochemistry, San Diego State University, San Diego, CA, USA
[2]The Smart Health Institute, San Diego State University, San Diego, CA, USA
*Correspondence: youngkwang.lee@sdsu.edu
‡A.J.S. and K.T. contributed equally to this work.

Supplementary Information

Supplementary Figures 1–27
Supplementary Table 1–3
Supplementary Text: Estimating kinetic rate constants involved in RAF membrane dissociation

1. Supplementary figures and tables

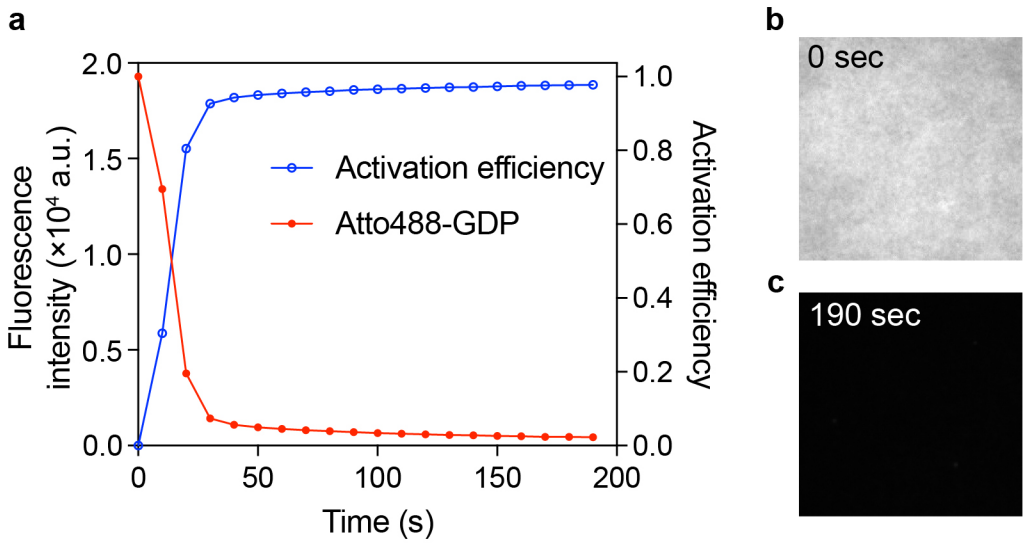

Supplementary Fig. 1: RAS activation via GTP nucleotide exchange using the SOS catalytic domain. a Fluorescence intensity (solid circles) of Atto488-GDP-bound RAS decreases over time as SOS replaces Atto488-GDP with unlabeled GTP. The activation efficiency (open circles) increases inversely to the fluorescence drop and is calculated by $|I_o - I(t)|/I_0$. **b,c** Fluorescence microscopy images of Atto488-GDP-bound RAS before (b) and after activation (c). Near-complete RAS activation is achieved within three minutes of SOS-mediated nucleotide exchange (SOS concentration: 100 nM). RAS density on the membrane is ~1200 μm^{-2}, and the membrane composition is 77% DOPC, 20% DOPS, and 3% MCC-DOPE. Source data are provided as a Source Data file. (n = 1 SLB)

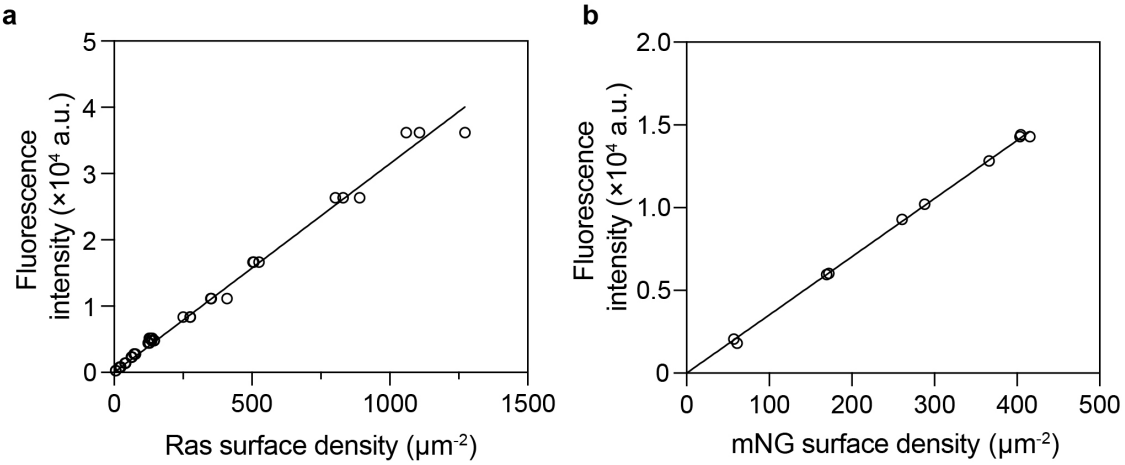

Supplementary Fig 2: TIRF calibration. The surface density of protein on supported membranes was determined by TIRF intensity, calibrated against FCS density measurements. **a** TIRF calibration of Atto488-GDP-labeled RAS**. b** TIRF calibration of His6-mNeonGreen (mNG) used for RAF-mNG constructs. The membrane composition is 77% DOPC, 20% DOPS and 3% MCC-DOPE for RAS calibration, and 96% DOPC and 4% NDG-NTA-DOPE for mNG calibration. The TIRF intensity was calculated by averaging values from nine positions (n = 9 field of views) acquired. Two FCS measurements (n = 2–4 focal spots) were performed per sample and are shown as individual data points (open circles). Solid lines represent a linear fit. Source data are provided as a Source Data file.

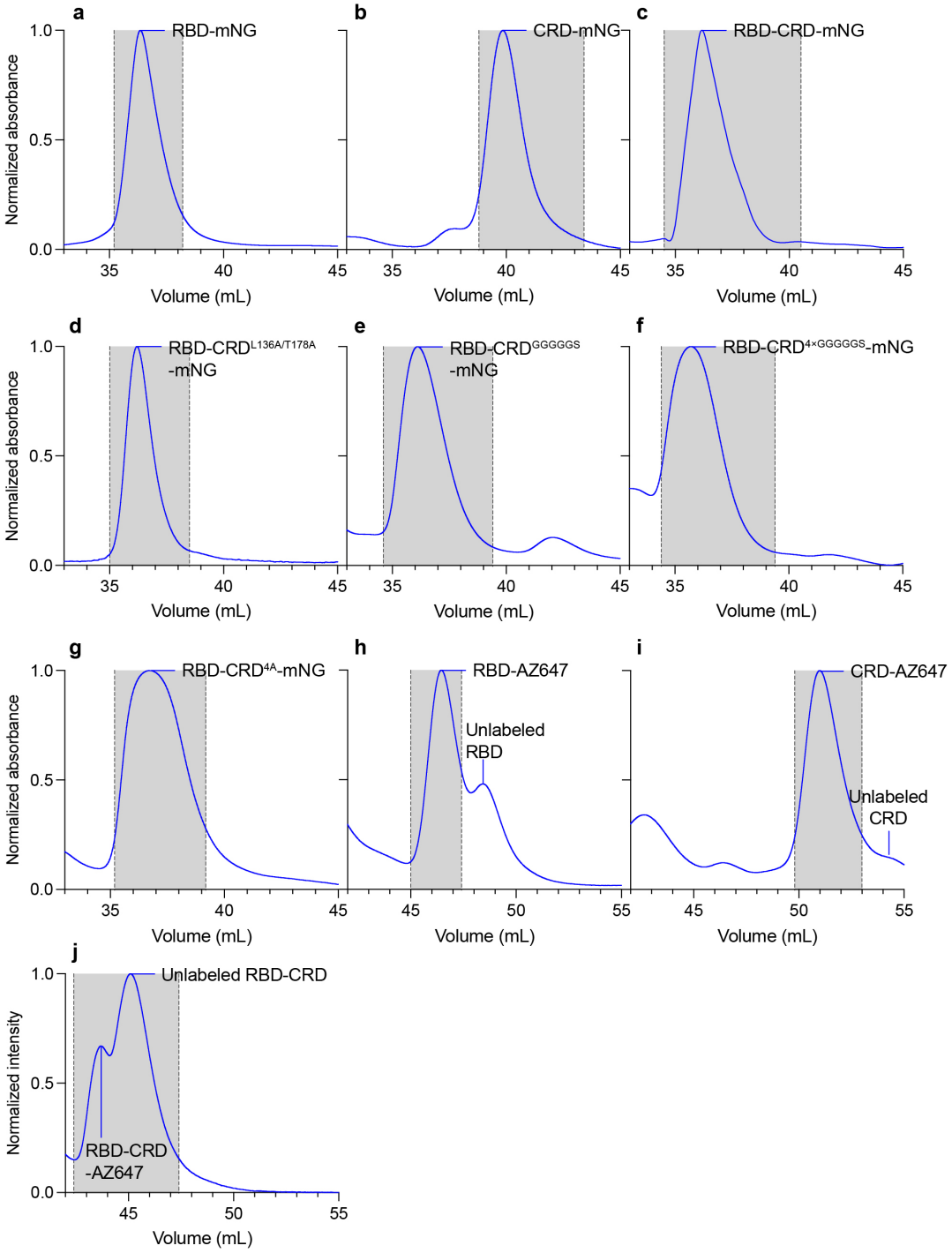

Supplementary Fig. 3: Size exclusion chromatography (SEC) chromatograms of RAF constructs. a–g RAF constructs fused with mNG. **h–j** RAF constructs labeled with AZ647 via sortase-mediated reactions. Normalized absorbance at 280 nm was used to display SEC chromatograms. Collected fractions are indicated by the grey shaded areas. Buffer compositions: 20 mM HEPES (pH 7.3), 500 mM NaCl, 1 mM TCEP, and 10% glycerol. All protein eluted at their expected elution volumes based on protein standards. Source data are provided as a Source Data file.

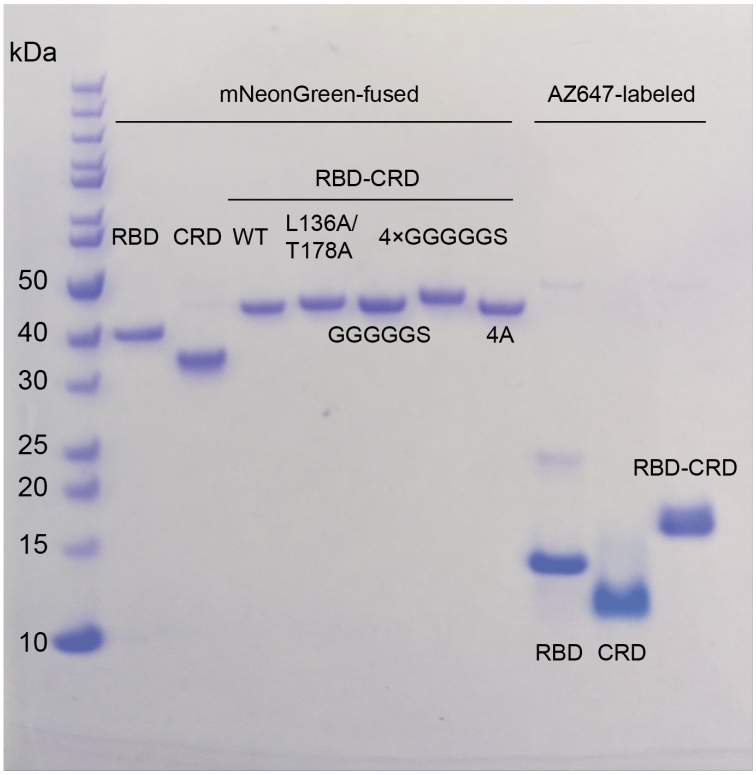

Supplementary Fig. 4: SDS–PAGE analysis of purified proteins used in this study. All protein bands were highly pure, except for RBD-AZ647, which contained minor detectable impurities. This impurity did not affect the single-molecule recruitment assays because samples were diluted according to the AZ647 label concentration and measured at dilute single-molecule densities. All bands migrated ~3–5 kDa above the expected molecular weight, likely due to intrinsic physicochemical properties of RBD and CRD; in SEC, all constructs eluted at the expected volumes relative to protein standards. All plasmids were verified by whole plasmid sequencing. Source data are provided as a Source Data file.

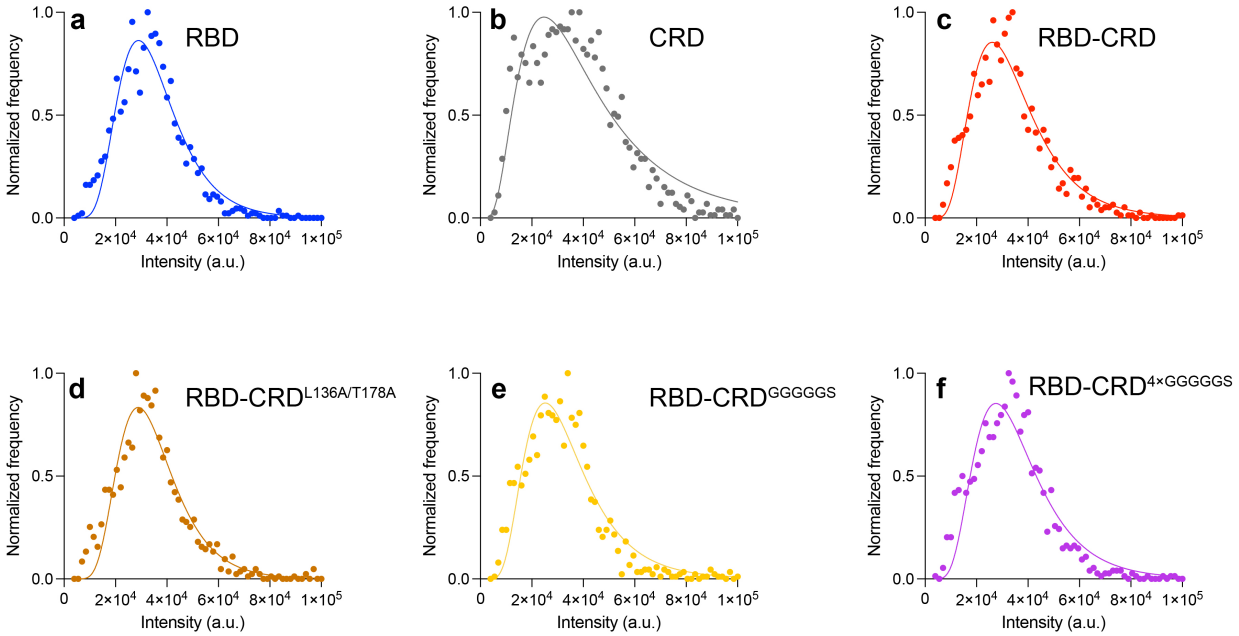

g

Constructs	Mean	SD ±
RBD	35724	23247
CRD	44165	32507
RBD-CRD	35184	23581
RBD-CRD$^{L136A/T178A}$	35410	23006
RBD-CRD^{GGGGGS}	34571	23296
RBD-CRD$^{4\times GGGGGS}$	36635	24448

Supplementary Fig. 5: Single-molecule intensity distributions of RAF-mNG constructs. a–f Normalized intensity distributions of RAF-mNG constructs. **g** Summary tables showing mean values and standard deviations estimated by a log-normal distribution corresponding to monomeric dispersity. All distributions (solid circles) were well described by a log-normal function (solid lines) except for the CRD, which exhibited an approximately 25% higher mean intensity and a broader distribution compared to other constructs. These results suggest that the CRD may contain a minor fraction of dimers. No high-intensity particles corresponding to larger oligomers were observed. All RAF molecules were diluted in HBS (40 mM HEPES, 150 mM NaCl, pH 7.4) supplemented with 5 mM $MgCl_2$ and nonspecifically immobilized to the glass surface. Each distribution was constructed from 500–1000 particles. Source data are provided as a Source Data file.

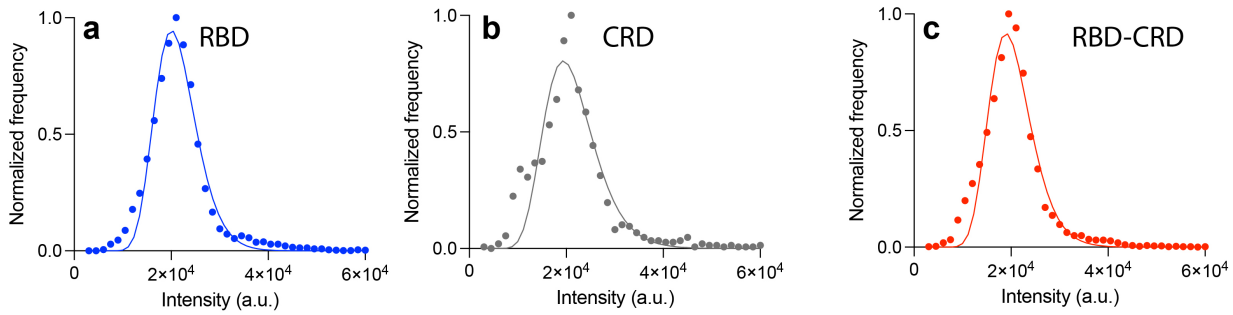

d

Constructs	Mean	SD ±
RBD	21412	13270
CRD	21422	13435
RBD-CRD	20432	12707

Supplementary Fig. 6: Single-molecule intensity distributions of RAF-AZ647 constructs. **a–c** Normalized intensity distributions of RAF-AZ647 constructs. **d** Summary tables showing mean values and standard deviations estimated by a log-normal distribution corresponding to monomeric dispersity. All distributions (solid circles) were well described by a log-normal function (solid lines). All RAF molecules were diluted in HBS (40 mM HEPES, 150 mM NaCl, pH 7.4) supplemented with 5 mM $MgCl_2$ and nonspecifically immobilized to the glass surface. Each distribution was constructed from 500–1000 particles. Source data are provided as a Source Data file.

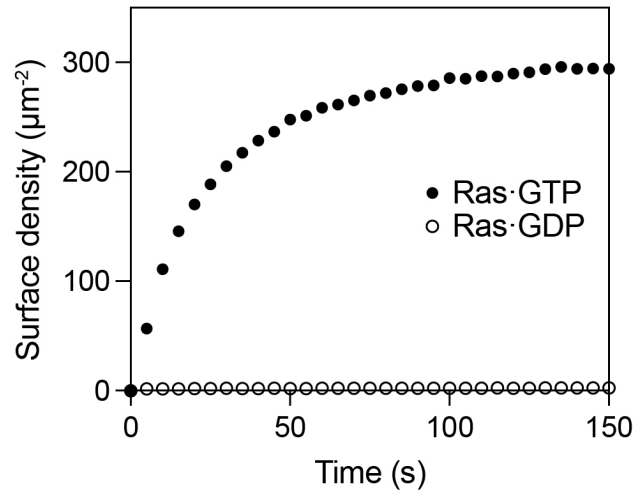

Supplementary Fig. 7: RBD-CRD-mNG binding on active and inactive RAS-functionalized membranes. Shown are the binding kinetics of RBD-CRD on supported membranes functionalized with RAS·GTP (~240 μm^{-2}) and RAS·GDP (~450 μm^{-2}). RBD-CRD displays robust binding to RAS·GTP membranes, whereas negligible binding is observed on RAS·GDP membranes. The membrane composition is 77% DOPC, 20% DOPS and 3% MCC-DOPE. Protein concentration: 20 nM. Source data are provided as a Source Data file.

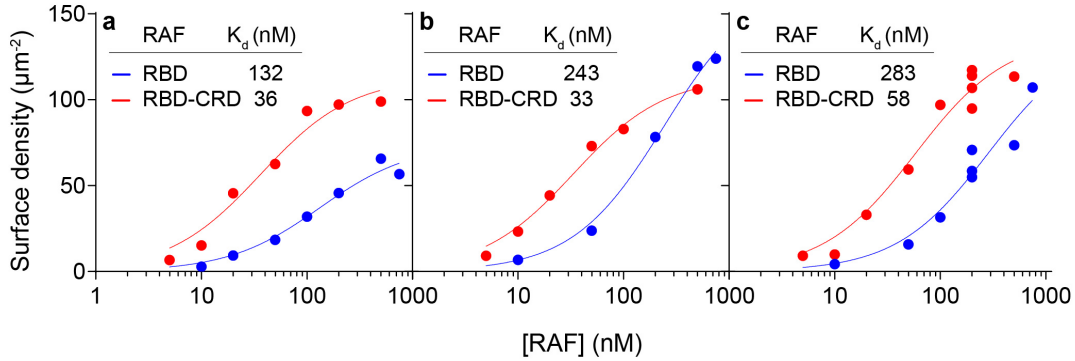

Supplementary Fig. 8: Determination of K_d for RAF binding to RAS on PEGylated glass surfaces. a–c Ttitration binding curves for RBD-mNG and RBD-CRD-mNG on HRAS-AviTag conjugated to a biotinylated PLL-PEG surface via streptavidin. The solid circles represent the equilibrium RAF surface densities. Solid lines indicate fits to a one-site saturation binding model. The average K_d values and standard deviations were determined to be 220 ± 80 nM for RBD and 40 ± 10 nM for RBD-CRD. The average K_d values and standard deviations were obtained from three independent experiments (N = 3) shown in (a), (b), and (c). RAS density: ~500 μm^{-2}. RAF surface densities did not reach those of RAS. This could be because a portion of RAS molecules was buried within the PLL–PEG polymer layer and thus inaccessible for RAF binding. This reduces the number of available binding sites without affecting the measured K_d values. Source data are provided as a Source Data file.

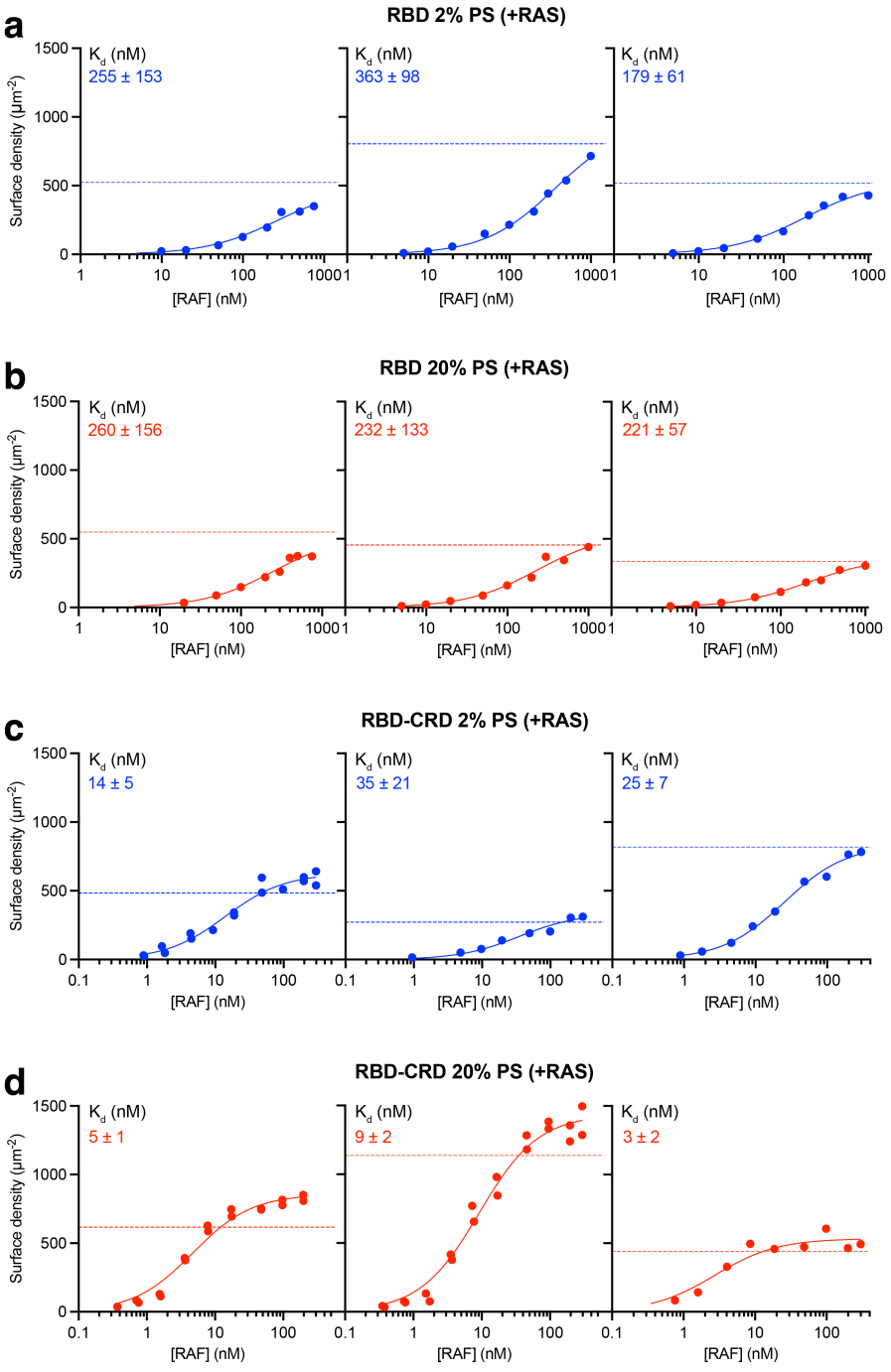

Supplementary Fig. 9: Determination of K_d for RAF binding to membrane-tethered RAS. **a–d** Titration binding curves of RAF-mNG constructs. The specific constructs and PS concentrations are indicated in each plot. The solid circles represent the equilibrium RAF surface densities. Solid lines indicate fits to a one-site saturation binding model.
The average K_d values for RBD were 270 ± 90 nM at 2% PS and 240 ± 20 nM at 20% PS. The average K_d values for RBD-CRD were 25 ± 10 nM at 2% PS and 6 ± 3 nM at 20% PS. Means values and standard deviations were obtained from three independent experiments (N = 3), which are shown as individual curves.

RAS surface densities are presented as a dashed line in each plot. The first column curves are presented as representative data in Figure 1e,f. Membrane composition: 77% DOPC, 20% DOPS and 3% MCC-DOPE or 97% DOPC, 2% DOPS and 1% MCC-DOPE. Source data are provided as a Source Data file.

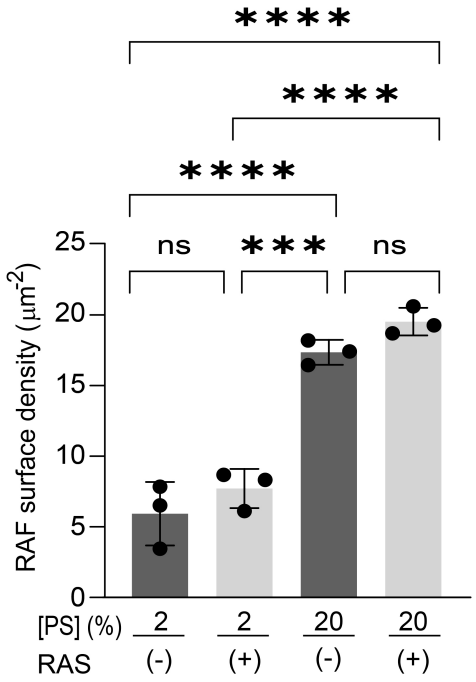

Supplementary Fig. 10: CRD-mNG binding on RAS-free and RAS-functionalized membranes containing 2% and 20% PS. Independent experiments reproduced similar results shown in Figure 1g. The mean surface densities (bars) and standard deviations (error bars) are obtained from three technical replicates (solid circles, n = 3 SLBs). Protein concentration: 300 nM. RAS density: 500 μm^{-2} for 2% PS and 650 μm^{-2} for 20% PS. Membrane composition: 98% DOPC and 2% DOPS or 80% DOPC and 20% DOPS for RAS-free membranes; 97% DOPC, 2% DOPS and 1% MCC-DOPE or 77% DOPC, 20% DOPS and 3% MCC-DOPE for RAS-functionalized membranes. One-way Anova followed by Tukey's multiple-comparisons test: α = 0.05; ***p<0.001; ****p<0.0001. Source data are provided as a Source Data file.

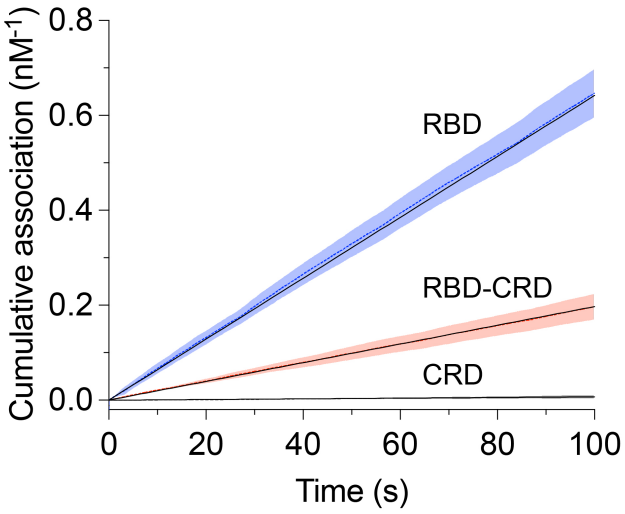

Supplementary Fig. 11: Cumulative RAF binding on RAS-functionalized membranes. A representative plot of cumulative RAF binding events over time (dashed lines) shows a linear increase, indicating a constant rate of binding. The apparent k_{on} value is determined from the slope of this linear fit (black solid lines), normalized by RAS density. Shaded bands indicate the standard deviation (n = 3 SLBs). The membrane composition is 77% DOPC, 20% DOPS and 3% MCC-DOPE. Protein concentrations were 50 pM for RBD and 200 pM for RBD-CRD and CRD, based on the concentration of the AZ647 label. RAS density: ~500 μm^{-2}. Source data are provided as a Source Data file.

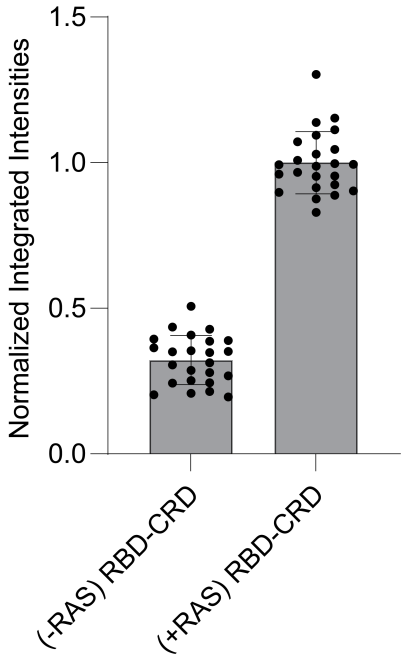

Supplementary Fig. 12: RBD-CRD exhibits highly transient short-lived interactions on RAS-free 20% PS membranes. The average integrated intensities (bars) and standard deviations (error bars) are calculated from 24 particles (n = 24 molecules). The intensities of single RBD-CRD-AZ647 particles (appearing as faint, diffusive traces) on RAS-free membranes were approximately threefold lower than those on RAS-functionalized membranes. Given a camera exposure time of 20 ms, these identifiable RBD-CRD-AZ647 molecules likely remain on the membrane for only several milliseconds. These highly transient interactions do not result in productive engagement (clearly spatially resolved bright spots) of RAS. Even shorter-lived species may exist but could not be detected under these conditions. Membrane composition: 80% DOPC and 20% DOPS for RAS-free SLBs; 77% DOPC, 20% DOPS, and 3% MCC-DOPE for RAS-functionalized SLBs. Source data are provided as a Source Data file.

Alpha	0.05	
Comparison	**Summary**	**P value**
RBD 2% PS vs. RBD 20% PS	ns	0.6321
RBD 2% PS vs. RBD-CRD 2% PS	ns	0.1299
RBD 2% PS vs. RBD-CRD 20% PS	ns	0.1655
RBD 2% PS vs. CRD 2% PS	***	0.0008
RBD 2% PS vs. CRD 20% PS	***	0.0009
RBD 20% PS vs. RBD-CRD 2% PS	*	0.0168
RBD 20% PS vs. RBD-CRD 20% PS	*	0.0213
RBD 20% PS vs. CRD 2% PS	***	0.0002
RBD 20% PS vs. CRD 20% PS	***	0.0002
RBD-CRD 2% PS vs. RBD-CRD 20% PS	ns	>0.9999
RBD-CRD 2% PS vs. CRD 2% PS	*	0.047
RBD-CRD 2% PS vs. CRD 20% PS	ns	0.05
RBD-CRD 20% PS vs. CRD 2% PS	*	0.0379
RBD-CRD 20% PS vs. CRD 20% PS	*	0.0403
CRD 2% PS vs. CRD 20% PS	ns	>0.9999

Supplementary Table 1. Statistical comparison of k_{on} values for RAF constructs measured on RAS-functionalized membranes containing either 2% or 20% PS (data shown in Figure 2b). Tukey's multiple comparisons test was used to evaluate differences in k_{on} values. Using a significance threshold $\alpha = 0.05$, the k_{on} for RBD on 20% PS was found to be significantly different from that for RBD-CRD on both 2% and 20% PS membranes. Although no statistically significant differences were observed for the k_{on} of RBD on 2% PS compared to RBD-CRD on 2% or 20% PS, its *p*-values were smaller than those of other non-significant comparisons. One-way ANOVA: ns>0.05; *p<0.05; **p<0.01; ***p<0.001.

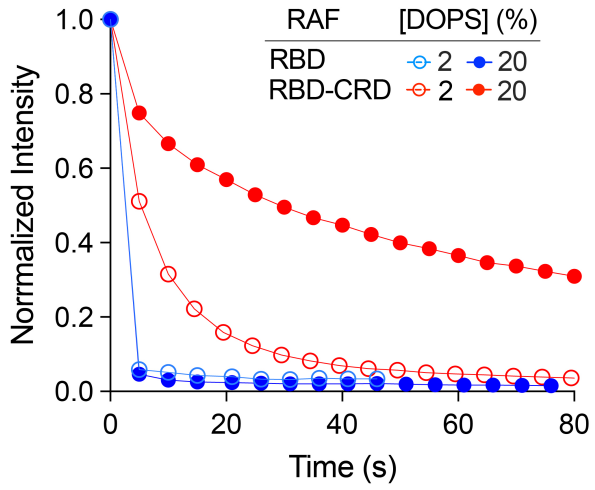

Supplementary Fig. 13: Ensemble free dissociation curves for RAF-mNG constructs on RAS-functionalized membranes containing 2% or 20% PS. Solid and open circles represent normalized time-lapse intensities. The curves were fit to a single-exponential decay to estimate half-lives, while the underlying dissociation mechanism is more complex as discussed later in this study. An independent experiment reproduced the results shown in Figure 2c. RBD-CRD exhibited slow dissociation kinetics compared to RBD in a PS-dependent manner. The half-life of RBD-CRD at 20% PS was ~30 seconds, which is shorter than that observed in Figure 2c due to the lower RAS surface density. The dependence of RBD-CRD dissociation kinetics on RAS density is discussed in Figure 5. Protein concentration: 50 nM. Membrane composition: 77% DOPC, 20% DOPS and 3% MCC-DOPE or 97% DOPC, 2% DOPS and 1% MCC-DOPE. RAS surface density: ~200 μm^{-2}. Source data are provided as a Source Data file.

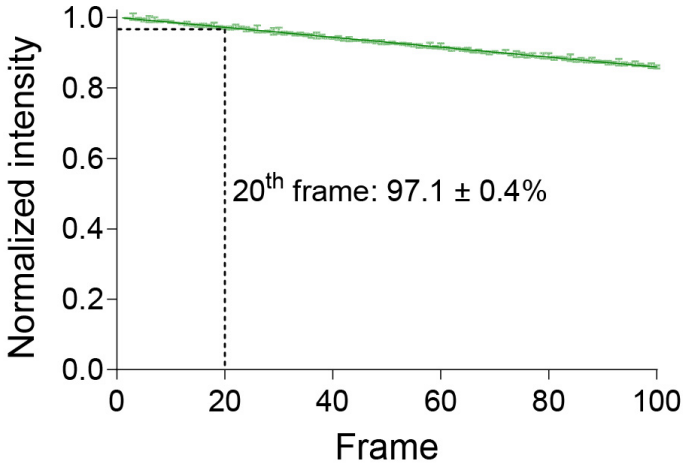

Supplementary Fig. 14: Photobleaching kinetics has a minimal impact on determining k_{off}. In our study, k_{off} was determined using an ensemble desorption assay, in which fluorescence intensity decay was measured at specified time intervals rather than by continuous streaming acquisition. Each measurement involved the acquisition of fewer than 20 frames. To quantify the contribution of photobleaching to the observed intensity decay, we measured the photobleaching kinetics of mNG stably tethered to supported lipid bilayers. The laser was illuminated every 0.5 seconds using the same laser power and exposure time as in the desorption assays. Only a minor photobleaching effect was observed over 100 frames, with a 3% decrease in fluorescence at the 20th frame, clearly demonstrating that photobleaching had little to no effect on our measurements. The average value (solid line) and standard deviations (error bars) were obtained from three technical replicates (n = 3 SLBs). Source data are provided as a Source Data file.

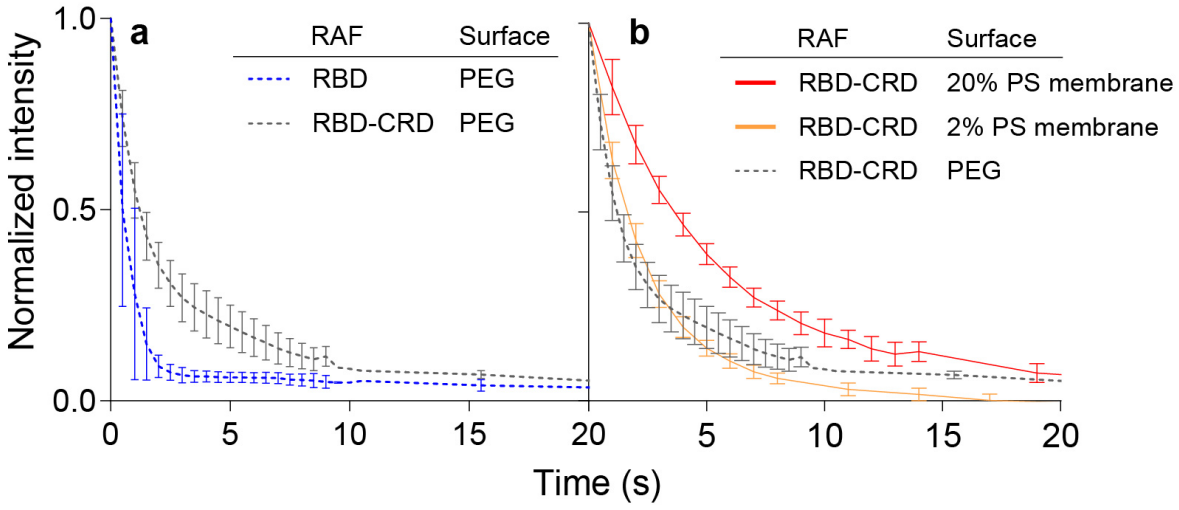

Supplementary Fig. 15: Dissociation kinetics of RBD and RBD-CRD from RAS on PEGylated glass surfaces. a Ensemble free dissociation kinetics of RBD-mNG and RBD-CRD-mNG from HRAS-Avitag conjugated to a biotinylated PEG surface via streptavidin In the absence of a lipid environment, RBD and RBD–CRD dissociated rapidly, with half-lives of only a few seconds. This rapid dissociation contrasts sharply with the slower dissociation observed on RAS-functionalized membranes (half-life of several tens of seconds; Fig. 2c and Supplementary Fig. 12). The RAS surface density was either ~500 or ~2000 μm^{-2}, and dissociation of both RBD and RBD–CRD from lipid-free PEG surfaces was independent of RAS density. The average values (dashed lines) and standard deviations (error bars) were obtained from five measurements (n = 5 SLBs) collected across at least three independent experiments (N ≥ 3). Protein concentration: 200 nM. **b** Comparison of the free dissociation kinetics of RBD-CRD-mNG from RAS on lipid-free PEG surfaces (shown in **a**) with the competitive FRET dissociation kinetics of RBD–CRD–AZ647 from RAS tethered to 2% or 20% PS membranes. The FRET dissociation data are reproduced from Figure 3b and Supplementary Figure 15a. See the source figure captions for statistical and experimental details. Membrane composition: 77% DOPC, 20% DOPS and 3% MCC-DOPE or 97% DOPC, 2% DOPS and 1% MCC-DOPE. Source data are provided as a Source Data file.

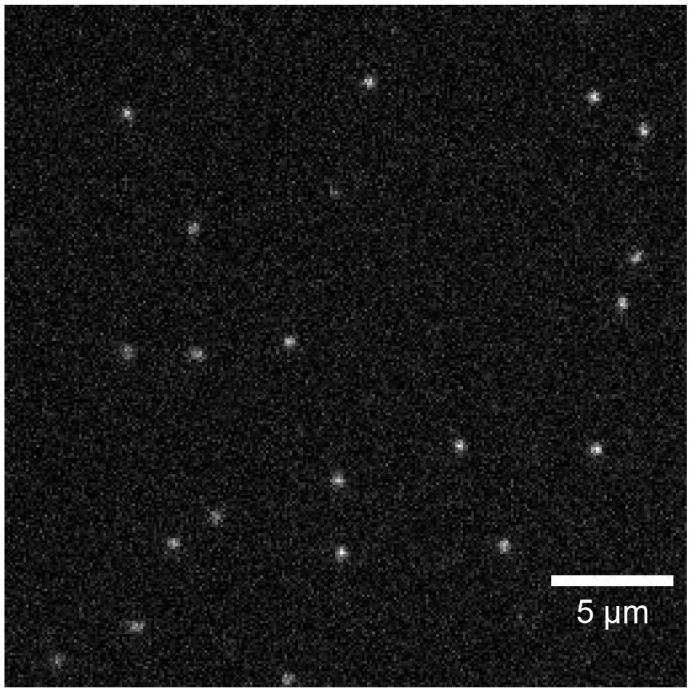

Supplementary Fig. 16: Representative snapshot image showing Alexa647-GppNp-labeld RAS. For single particle tracking of RAS, a small population of RAS was labeled with Alexa647-GppNp, ensuring a well-dispersed single-molecule density (~20–30 particles per region of interest). Membrane composition: 77% DOPC, 20% DOPS and 3% MCC-DOPE. Total Ras density: ~550 μm^{-2}. Source data are provided as a Source Data file.

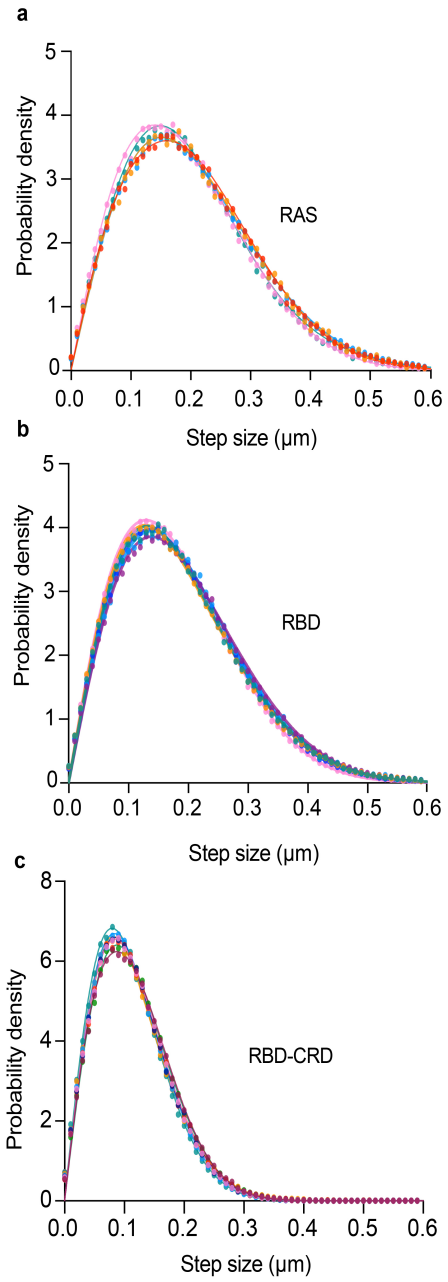

d

Construct	HRAS184		
Sample #	D_1	D_2	α
1	0.58	0.15	0.94
2	1.06	0.27	0.92
3	1.14	0.14	0.97
4	1.20	0.38	0.91
5	1.27	0.49	0.85
Mean	1.05	0.29	0.92
SD ±	0.27	0.15	0.05

e

Construct	RBD		
Sample #	D_1	D_2	α
1	1.13	0.41	0.82
2	1.09	0.41	0.84
3	1.10	0.39	0.87
4	1.09	0.36	0.80
5	1.01	0.28	0.91
6	0.94	0.25	0.91
Mean	1.06	0.34	0.86
SD ±	0.07	0.06	0.04

f

Construct	RBD-CRD		
Sample #	D_1	D_2	α
1	0.39	0.14	0.90
2	0.39	0.08	0.95
3	0.37	0.12	0.92
4	0.40	0.17	0.81
5	0.40	0.16	0.84
6	0.38	0.16	0.82
7	0.43	0.18	0.72
8	0.36	0.13	0.85
Mean	0.39	0.14	0.85
SD ±	0.02	0.03	0.07

Supplementary Fig. 17: Diffusion analysis of RAS and RAF on 20% PS membranes. Individual step size distributions of **a** RAS, **b** RBD, and **c** RBD-CRD used to calculate the average step size distributions and their standard deviations shown in Figure 2e. Each distribution (solid circles) was fit to a two-species random diffusion model (solid lines). **d–f** Summary table for estimated diffusion coefficients for the fast species (D_1), the slow species (D_2), and the fraction of the fast species (α). The data were collected at least two independent experiments (N = 2). Apparent diffusion coefficients ($\mu m^2/s$), calculated by the weighted average of D_1 and D_2, are 0.99 for RAS, 0.96 for RBD, and 0.35 for RBD–CRD. RAS surface density: ~250-900 μm^{-2}. Membrane composition: 77% DOPC, 20% DOPS and 3% MCC-DOPE. See the Figure 2e caption for experimental details. Source data are provided as a Source Data file.

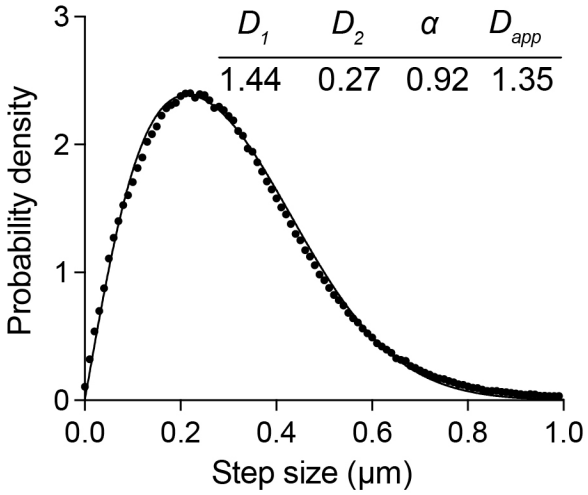

Supplementary Fig. 18: Step size distribution of Atto565-DOPE lipids on a supported lipid bilayer. The distribution (solid circles) was fit to a two-species random diffusion model (solid line). The lipids exhibit two distinct diffusion populations, with the majority species (>90%) diffusing at 1.44 μm²/s. The membrane composition is 80 mol% DOPC, 20 mol% DOPS, and $1x10^{-5}$ mol% Atto565–DOPE. Images were recorded with a time interval of 10 ms. Diffusion coefficients for the fast species: D_1; the slow species: D_2; the fraction of the fast species: α; n = 1 SLB. Source data are provided as a Source Data file.

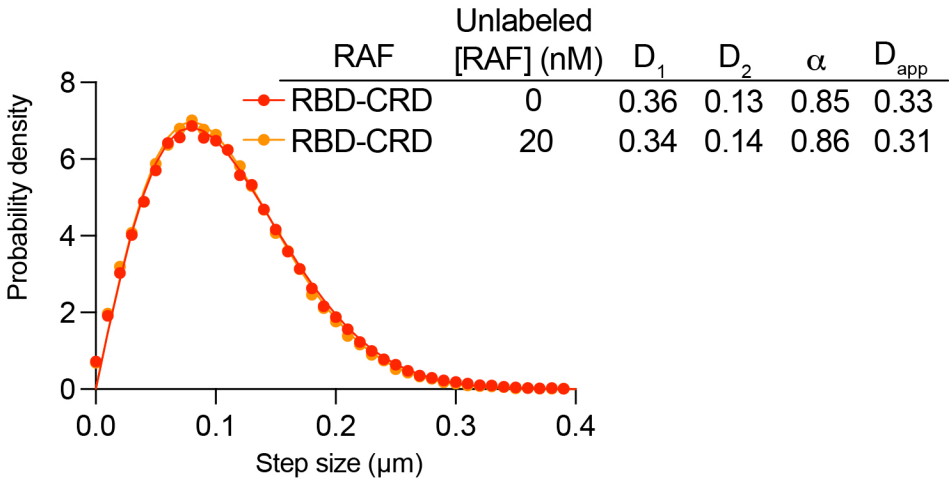

Supplementary Fig. 19: Diffusion analysis of RBD-CRD in the absence and presence of excess unlabeled RAF. Each distribution (solid circles) was fit to a two-species random diffusion model (solid lines). Diffusion of RBD-CRD remain unchanged at a saturating concentration of unlabeled RBD-CRD (20 nM), confirming that the slower diffusion observed

relative to RBD in Fig. 2e is due to lipid interactions with individual RAS:RBD-CRD complexes rather than collective behaviors such as clustering. The experiments were performed on membranes composed of 77% DOPC, 20% DOPS and 3% MCC-DOPE, functionalized with RAS at a density of ~400 μm^{-2}. Protein concentration: 10 pM and 100 pM of RBD-CRD-AZ647 (based on the concentration of the AZ647 label) were used for experiments without and with unlabeled RBD-CRD,respectively. The images were acquired with a 10 ms time interval. Diffusion coefficients for the fast species: D_1; the slow species: D_2; the fraction of the fast species: α; n = 1 SLB. Source data are provided as a Source Data file.

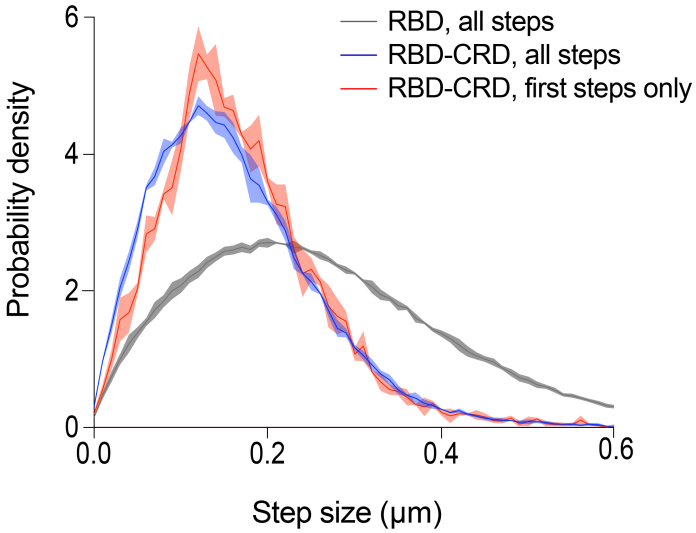

Supplementary Fig. 20: Distribution of RAF at different time ranges. RBD-CRD displays similar diffusion during the initial steps of trajectories (first steps) and across the entire trajectories (all steps). The experiments were performed on membranes composed of 77% DOPC, 20% DOPS and 3% MCC-DOPE. RAS density is ~350 μm^{-2} for both RBD-CRD and RBD measurements. To minimize blinking effects, the experiments were conducted under fast bleaching conditions in the absence of glucose oxidase/catalase imaging buffer, with 1 mM BME added to eliminate potential oxidative photo effects. Images were acquired with a 20 ms time interval. Protein concentrations: 50 pM for RBD and RBD-CRD based on the concentration of the AZ647 label. The average diffusion step size distributions (solid line) and standard deviations (shaded area) are calculated from three technical replicates (n = 3 SLBs). Source data are provided as a Source Data file.

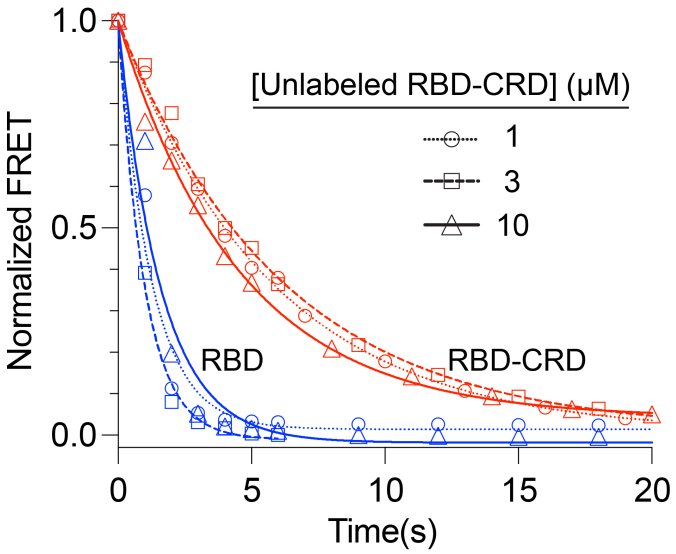

Supplementary Fig. 21: Competitive FRET dissociation kinetics for RAF-AZ647 constructs with different concentrations of unlabeled RBD-CRD. Open symbols and lines represent normalized time-lapse FRET intensities and single-exponential fits, respectively. Competitive FRET dissociation experiments between RAF-AZ647 and Atto488-GppNp-RAS were performed in the presence of unlabeled RBD-CRD at concentrations ranging from 1 to 10 μM. All tested micromolar concentrations of unlabeled RBD-CRD are equally efficient at sequestering free RAS upon dissociation of RAF-AZ647 (RBD in blue; RBD-CRD in red). The experiments were conducted on membranes composed of 77% DOPC, 20% DOPS and 3% MCC-DOPE. Ras density is ~400 μm^{-2} for RBD and RBD-CRD measurements. Protein concentration: 200 nM for RBD-AZ647 and 20 nM RBD-CRD-AZ647 based on the protein concentration, determined from absorbance at 280 nm. Source data are provided as a Source Data file.

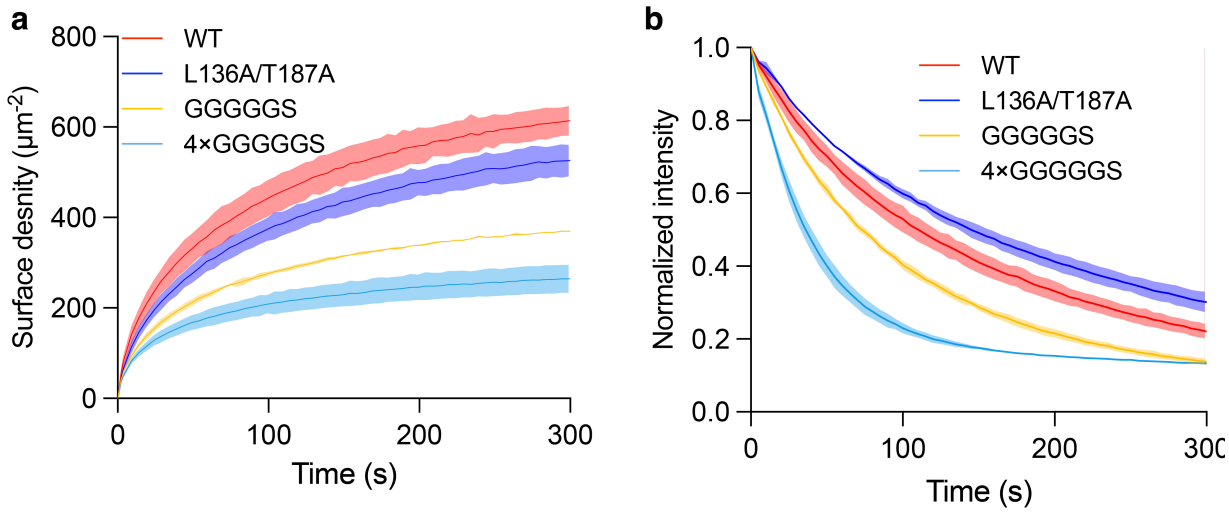

Supplementary Fig. 22: Role of linker in RBD-CRD membrane binding. a Ensemble binding and **b** free desorption kinetics of WT RBD-CRD, the L136A/T178A mutant, and linker variants. An independent experiment showed the similar results shown in Figure 4. The average (solid line) and standard deviation (shaded region) were obtained from two technical replicates (n = 2 SLBs). Protein concentration: 10 nM. RAS surface density: ~700 μm^{-2}. Membrane composition: 77% DOPC, 20% DOPS and 3% MCC-DOPE. Source data are provided as a Source Data file.

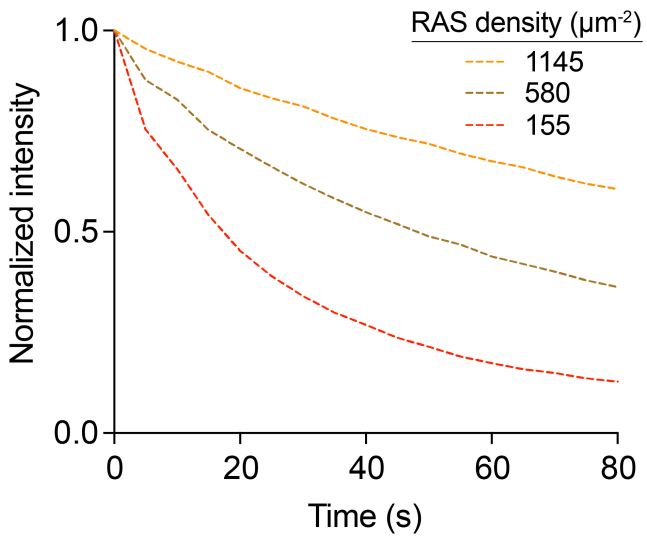

Supplementary Figure 23. The dependence of RBD-CRD dissociation on RAS density. Dashed lines indicate normalized time-lapse intensities. An independent experiment reproduced the extended membrane residence of RBD-CRD at higher RAS densities, consistent with Figure 5d. RBD-CRD concentration: 20 nM. Membrane composition: 77% DOPC, 20% DOPS and 3% MCC-DOPE. Source data are provided as a Source Data file.

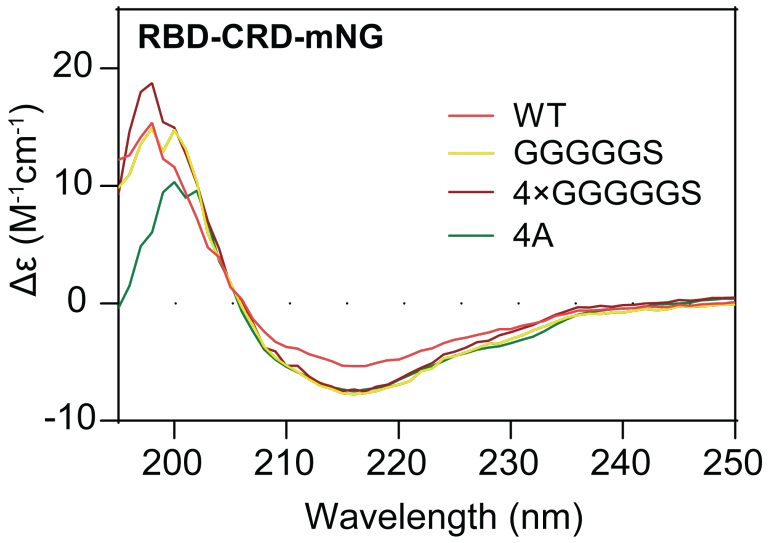

Supplementary Fig. 24: Far-UV circular dichroism (CD) spectra of mNG-fused RBD-CRD constructs. Prior to measurements the buffer was exchanged to 10 mM Tris (pH7.4) and 150 mM NaF using a desalting column to improve the overall quality of the spectra. The CD spectra (solid curves) of WT RBD-CRD, RBD-CRD linker variants (GGGGGS and 4×GGGGGS), and the RBD-CRD containing tetra-alanine mutations (K148A, L149A, K157A, and F158A; hereafter referred to as 4A) showed a negative peak at ~216 nm, characteristic of an antiparallel β-sheet secondary structure present in both RBD-CRD and mNG. WT RBD-CRD, which exhibits the highest membrane binding, showed a slightly lower CD intensity. Source data are provided as a Source Data file.

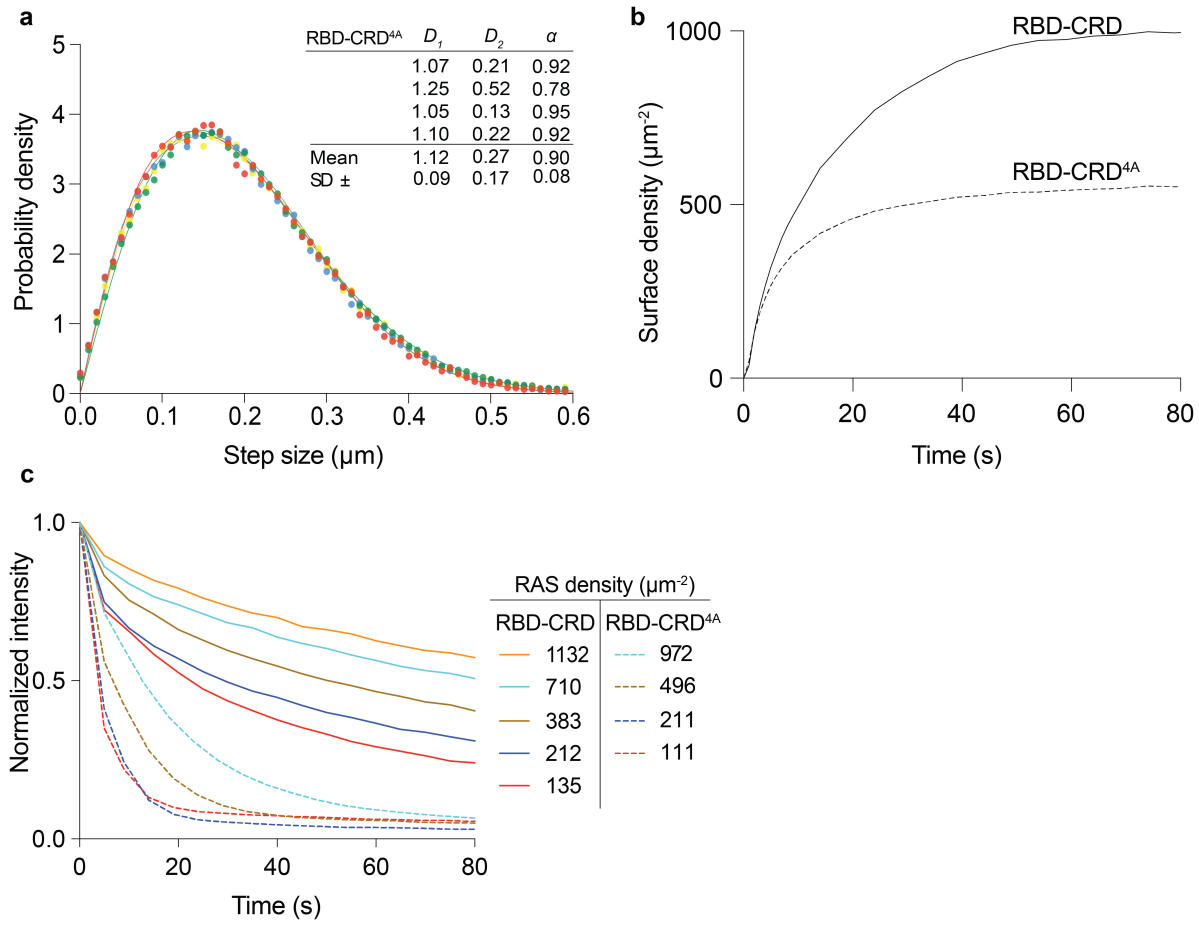

Supplementary Fig. 25: Characterization of the RBD-CRD^{4A}-mNG construct on RAS-functionalized membranes containing 20% PS. a Diffusion analysis. Each dataset (open circles) was individually fitted, with solid lines representing the fitted curves and dots indicating the raw data points (n = 4 SLBs). The apparent diffusion coefficient, calculated by the weighted average of D_1 and D_2, of RBD-CRD^{4A} was determined to be 1.03 μm^2/s, which is close to that of RBD (0.96 μm^2/s, shown in Supplementary Fig. 17). Protein concentration: 50 pM based on the mNG concentration. RAS density: ~290 μm^{-2}. **b** Ensemble membrane binding kinetics (solid and dashed lines) of WT RBD-CRD and RBD-CRD^{4A}. RBD-CRD binds more strongly than the mutant RBD-CRD4A, highlighting the importance of intact CRD lipid-interacting residues. Protein concentration: 50 nM. RAS density: ~950 μm^{-2}. **c** Free desorption kinetics of WT RBD-CRD (solid curves) and RBD-CRD^{4A} (dashed curves) were measured across a range of RAS densities (~100–1100 μm^{-2}). The dissociation kinetics of RBD-CRD^{4A} were faster compared to WT RBD-CRD and exhibited a weaker dependence on RAS density. The dissociation kinetics of RBD-CRD^{4A} remained unchanged at RAS densities of 111 and 211 μm^{-2} and showed only a modest change at 496 μm^{-2}, whereas those of WT RBD-CRD exhibited a clear dependence as RAS density increased from 135 to 212 to 383 μm^{-2}, These results indicate that disruption of CRD–lipid interaction attenuates lateral rebinding and overall membrane association. Protein concentration: 20 nM for WT RBD-CRD; 50 nM for RBD-CRD^{4A}. Source data are provided as a Source Data file.

2. Estimating kinetic rate constants involved in RAF membrane dissociation

Based on our experimental findings, we propose the following reaction scheme to describe how the CRAF RBD-CRD associate with the membrane:

Step	Reaction	Rate constants
(1)	RAS(m) + RBD-CRD(s) ↔ RAS:RBD-CRD(m)	k_1/k_{-1} fwd/rev rate constants
(2)	RAS:RBD-CRD(m) + PS(m) → RAS:RBD-CRD:PS(m)	k_2 fwd rate constant
(3)	RAS:RBD-CRD:PS(m) ↔ RAS(m) + RBD-CRD:PS(m)	k_3/k_{-3} fwd/rev rate constants
(4)	RBD-CRD:PS(m) → RBD-CRD(s) + PS(m)	k_4 fwd rate constant

(m) and (s) denote the membrane and solution phases, respectively.

The initial step involves RBD binding to membrane-bound RAS, forming RAS:RBD-CRD on the membrane (1). Once the RBD-CRD is membrane-associated via RBD–RAS interaction, the CRD engages lipids (e.g., PS) to form RAS:RBD-CRD:PS (2). We did not observe the reverse reaction of step (2) in our experimental conditions. Dissociation begins with RAS unbinding, creating a transient RBD-CRD:PS intermediate that can laterally rebind to RAS (3) or proceed to the final unbinding step. In the final step, the CRD detaches from the membrane lipid PS (4). The reverse reaction of step (4) was negligible at the concentration used in dissociation assays (20 nM). The stoichiometry between CRD and PS is not well-defined because its promiscuous nature that relies on multiple interdigitated positively charged and hydrophobic residues. For simplicity, we therefore treated this interaction effectively monovalent, representing the convoluted multivalent binding with an apparent rate constant. Overall, the model describes a two-step association (steps 1 and 2) followed by two sequential dissociation steps (steps 3 and 4).

For the free dissociation experiments, only steps (3) and (4) of our reaction scheme are relevant. The corresponding rate laws for these steps are:

$$d[RAS]/dt = k_3[RAS{:}\,RBD\text{-}CRD{:}\,PS] - k_{-3}[RAS][RBD\text{-}CRD{:}\,PS]$$
$$d[RBD\text{-}CRD]/dt = k_4[RBD\text{-}CRD{:}\,PS]$$
$$d[PS]/dt = k_4[RBD\text{-}CRD{:}\,PS]$$
$$d[RBD\text{-}CRD{:}\,PS]/dt = k_3[RAS{:}\,RBD\text{-}CRD{:}\,PS] - k_{-3}[RAS][RBD\text{-}CRD{:}\,PS] - k_4[RBD\text{-}CRD{:}\,PS]$$
$$d[RAS{:}\,RBD\text{-}CRD{:}\,PS]/dt = -k_3[RAS{:}\,RBD\text{-}CRD{:}\,PS] + k_{-3}[RAS][RBD\text{-}CRD{:}\,PS]$$

Three kinetic constants—k_3, k_{-3} and k_4—are involved. We first estimated k_3 by fitting the competitive FRET dissociation assay data. These assays monitor only the dissociation of RAS from the RAS:RBD-CRD:PS complex while preventing the reverse reaction by including an excess of unlabeled RBD-CRD, which sequesters free RAS. Under these conditions, the dissociation of RAS can be treated as an irreversible unimolecular reaction:

RAS:RBD-CRD:PS(m) → RAS(m) + RBD-CRD:PS(m) (k_3 fwd rate constant)

By fitting the FRET dissociation curves obtained from TIRF measurements, we estimated k_3 to be 0.18 s^{-1} (**Supplementary Fig. 10**). This value corresponds to the unimolecular rate constant for RAS dissociation from the membrane-bound RAS:RBD-CRD:PS complex.

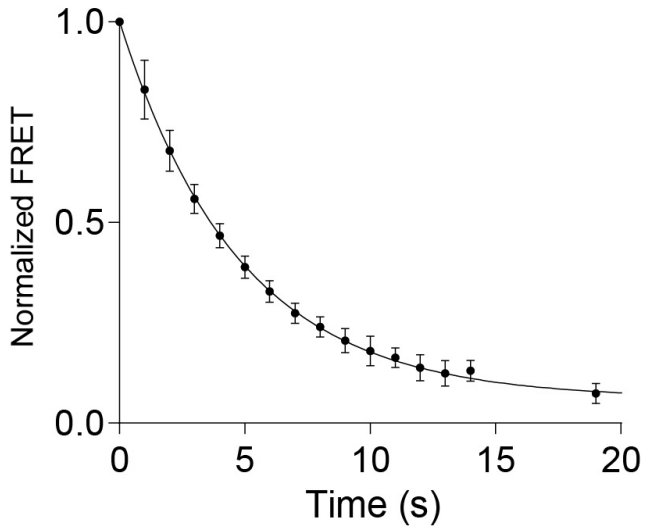

Supplementary Fig. 26: Competitive FRET dissociation curve fit. The solid line and error bars represent the average values and standard deviations, respectively. The data was fit with an irreversible unimolecular dissociation kinetic model: $y(t) = e^{-k_3 t}$. k_3 was estimated to be 0.21 s^{-1}. The experiments were conducted on membranes composed of 77% DOPC, 20% DOPS and 3% MCC-DOPE (n = 6 SLBs. N = 3 independent experiments). Ras density is ~500 μm^{-2}. Protein concentration: 20 nM RBD-CRD based on the protein concentration determined from absorbance at 280 nm. Source data are provided as a Source Data file.

The rate constants k_{-3} and k_4 were determined by fitting RBD-CRD free dissociation data obtained at different RAS surface densities. Under these conditions, the membrane-bound forms of RBD-CRD are RAS:RBD-CRD:PS and RBD-CRD:PS. The sum of these two species were optimized to estimate k_{-3} and k_4. Except for RBD-CRD that dissociates into solution, all species involved in the reaction remain membrane-bound. Because free RBD-CRD escapes the system due to continuous buffer rinsing, the amounts of all membrane-bound species can be expressed in terms of their surface density (μm^{-2}). For each dissociation assay, we experimentally determined the surface densities of RAS and membrane-bound RBD-CRD. The assays were performed at 20 nM RBD-CRD which barely saturate RAS. Therefore, we assume that RBD-CRD exists predominantly as RAS:RBD-CRD:PS unless its density exceeds that of RAS. This assumption is supported by data showing that more than 100 nM RBD-CRD is required to observe a substantial amount of RAS-free RBD-CRD (Fig. 1f). Based on our experimental measurements, the following initial conditions were used for curve fitting:

Total Ras (μm^{-2})	RAS:RBD-CRD:PS (μm^{-2})	RBD-CRD:PS (μm^{-2})
1132	1132	47
710	710	8
383	383	39
207	207	4
141	135	0

Supplementary Table 2. Surface densities of membrane-bound species used for the initial conditions of RBD-CRD free dissociation curve fitting.

The following table summarizes the estimated kinetic constants:

Reaction	Forward rate constant	Reverse rate constant
RAS:RBD-CRD:PS(m) ↔ RAS(m) + RBD-CRD:PS(m)	k_3 = 0.21 s^{-1}	k_{-3} = 0.044 $\mu m^2 s^{-1}$
RBD-CRD:PS(m) → RBD-CRD(s) + PS(m)	k_4 = 0.38 s^{-1}	N/A

Supplementary Table 3. Estimated kinetic constants for RBD-CRD dissociation

We used the kinetic constants shown in Supplementary Table 2 for kinetic simulations in Figure 5c. Kinetic modeling and kinetic constant estimation were performed in SimBiology (Mathworks) by numerically solving the rate equations using ODE45.

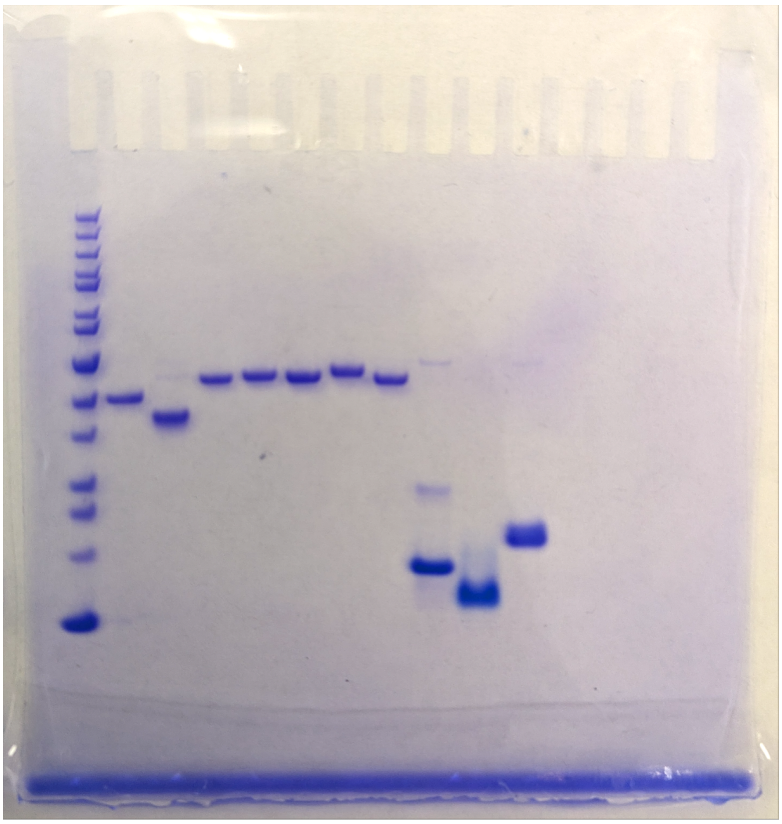

Supplementary Fig. 27: Uncropped SDS–PAGE gel in Supplementary Fig 4.